

## Research



**Cite this article:** Reynolds TPS, Burrigge HC, Johnston R, Wu G, Shah DU, Scherman OA, Linden PF, Ramage MH. 2018 Cell geometry across the ring structure of Sitka spruce.

*J. R. Soc. Interface* **15**: 20180144.

<http://dx.doi.org/10.1098/rsif.2018.0144>

Received: 28 February 2018

Accepted: 20 April 2018

**Subject Category:**

Life Sciences—Engineering interface

**Subject Areas:**

biomaterials, bioengineering

**Keywords:**

wood, timber, morphometry, X-ray computed tomography, microstructure, flow

**Author for correspondence:**

T. P. S. Reynolds

e-mail: [t.reynolds@ed.ac.uk](mailto:t.reynolds@ed.ac.uk)

Electronic supplementary material is available online at <https://dx.doi.org/10.6084/m9.figshare.c.4088579>.

## Cell geometry across the ring structure of Sitka spruce

T. P. S. Reynolds<sup>1</sup>, H. C. Burrigge<sup>2</sup>, R. Johnston<sup>3</sup>, G. Wu<sup>4</sup>, D. U. Shah<sup>5</sup>, O. A. Scherman<sup>4</sup>, P. F. Linden<sup>6</sup> and M. H. Ramage<sup>5</sup>

<sup>1</sup>Institute for Infrastructure and Environment, School of Engineering, University of Edinburgh, Edinburgh EH9 3FG, UK

<sup>2</sup>Department of Civil and Environmental Engineering, Imperial College London, London SW7 2AZ, UK

<sup>3</sup>Materials Research Centre, College of Engineering, Swansea University, Swansea SA1 8EN, UK

<sup>4</sup>Melville Laboratory for Polymer Synthesis, Department of Chemistry, University of Cambridge, Lensfield Road, Cambridge CB2 1EW, UK

<sup>5</sup>Department of Architecture, University of Cambridge, Cambridge CB2 1PX, UK

<sup>6</sup>Department of Applied Mathematics and Theoretical Physics, University of Cambridge, Centre for Mathematical Sciences, Wilberforce Road, Cambridge CB3 0WA, UK

TPSR, 0000-0002-6754-9183; HCB, 0000-0002-0719-355X; RJ, 0000-0003-1977-6418; GW, 0000-0002-9690-5992; DUS, 0000-0002-8078-6802; OAS, 0000-0001-8032-7166

For wood to be used to its full potential as an engineering material, it is necessary to quantify links between its cell geometry and the properties it exhibits at bulk scale. Doing so will make it possible to predict timber properties crucial to engineering, such as mechanical strength and stiffness, and the resistance to fluid flow, and to inform strategies to improve those properties as required, as well as to measure the effects of interventions such as genetic manipulation and chemical modification. Strength, stiffness and permeability of timber all derive from the geometry of its cells, and yet current practice is to predict them based on properties, such as bulk density, that do not directly describe the cell structure. This work explores links between micro-computed tomography data for structural-size pieces of wood, which show the variation of porosity across the wood's ring structure, and high-resolution tomography showing the geometry of the cells, from which we measure cell length, lumen area, porosity, cell wall thickness and the number density of cells. High-resolution scans, while informative, are time-consuming and expensive to run on a large number of samples at the scale of building components. By scanning the same volume of timber at both low and high resolutions (high-resolution scans over a near-continuous volume of timber of approx.  $20\text{ mm}^3$  at  $15\text{ }\mu\text{m}^3$  per voxel), we are able to demonstrate correlations between the measurements at the two different resolutions, reveal the physical basis for these correlations, and demonstrate that the data from the low-resolution scan can be used to estimate the variation in (small-scale) cell geometry throughout a structural-size piece of wood.

## 1. Background and summary

The internal structure of a softwood like Sitka spruce makes it effective both as a conduit for fluid transport and as a structural material: multifunctional tracheid cells with high aspect ratio make up over 90% of the volume of the wood, and provide a flow path through their lumina, and structural support through a thickened secondary cell wall. Groups of ray cells allow fluid flow in the radial direction and resin ducts form in spaces between cells. All these cells contribute to the structural and flow performance of the wood. The scale of both the lumina and the cell walls varies depending on the stage of the growing season at which a particular portion of the wood was laid down. Wood laid down early in the growing season, the so-called 'earlywood', contains larger lumina and thinner cell walls than that of 'latewood' and as such is expected to exhibit different structural and fluid transport properties [1].

The empty lumina in dry wood make it a lightweight and efficient structural material, with a strength-to-weight ratio along the axis of the trunk comparable to that of steel [2]. In the use of wood for engineering, the flow paths, as well as the structural resistance, are important: wood can be impregnated with fluid treatments for preservation, or to enhance its performance. Few treatment processes achieve any substantial degree of impregnation, however, with most wood treatment occurring at or near surface. Accurate modelling of flow is required to design treatment processes, which in turn requires a thorough understanding of cell geometry.

Measurement of cell geometry can also improve understanding of the load resistance of wood [3,4]. Gibson [4] describes how plants achieve a wide range of mechanical properties by alterations to this geometry as well as changes to the composition of the cell wall. Qing & Mishnaevsky [5] present a series of numerical models extending from the arrangement of cellulose in the cell wall through the shape of tracheid cells to the ring structure in a softwood. Malek & Gibson [6] present numerical models which also incorporate the effect of other cell types to bring out the nonlinear relationship between density and elastic modulus in balsa wood. Such research enables the development of relationships between cell geometry and bulk structural properties of timber [6–10]. This well-developed field of research shows the promise that if the geometry of cells can be accurately measured, then, in conjunction with information about the molecular architecture of the cell wall, the strength and stiffness of wood can be predicted. Microtomography of timber at the structural scale cannot currently measure cell geometry directly, but using a suitable relationship between larger-scale microtomography and cell geometry, a prediction of bulk structural properties could be possible. This study proposes such a relationship and demonstrates how it can be applied to Sitka spruce softwood.

A multi-scale understanding of the geometry of wood can enable the development of new wood products which make the best use of the natural structure of the material, and could also improve the process of timber grading. Grading structural timber requires properties that can be measured quickly and without damage, the *indicating properties*, which correlate well with the strength and stiffness properties of the timber [11], some of which cannot be measured without damaging the material. The present process of grading structural timber uses properties such as bulk density and bending stiffness as indicating parameters, but cell geometry would seem a promising candidate, because it represents a more fundamental property of the wood, and *in situ* loading with micro-tomography has enabled observation of behaviour of the cells responsible for structural failure of wood [12,13]. A commercial system now exists for X-ray computed tomography (CT) scanning of logs prior to sawmilling [11], which suggests that its large-scale implementation in grading could be economically feasible.

To realize the potential for accurate prediction of the properties of structural timber based on measurements correlated with cell geometry, it is necessary to make a link between measurements made at the bulk scale on structural-size pieces of timber, and those that can distinguish and measure individual cells. This study uses X-ray micro-CT ( $\mu$ CT) to construct an image of the internal structure of Sitka spruce, *Picea sitchensis*, at those two scales.

Previous studies using CT scanning of plant material can be divided into those concerned with the cell structure of the material, and those concerned with larger features. Studies of larger features investigate knots and splits in sawn timber [14], adhesive joints in glued-laminated timber [15], and fluid content [16] or transport of fluid through wood [17]. These studies use spatial resolutions in the range of 100–400  $\mu$ m and, therefore, only show the variation in density across the growth rings in a softwood, but do not distinguish cell walls.

Microtomography of the cellular structure, on the other hand, has been used to measure the penetration of adhesive or other fluids [15,18], the mechanisms in the cells which control the movement of fluid [19,20] and the response of the individual cells to applied load [21]. As hardwood has vessels that have a relatively large cross-sectional area, they were the first to be distinguished as X-ray microtomography developed. Steppe *et al.* [22] measure vessel geometry in hardwoods by an image segmentation technique, with results verified by inspection and direct measurement from the images. Image segmentation was later applied to the more densely packed tracheid cells in softwood [23] and the fibre, ray and vessel cells in hardwood [18]. Sedighi Moghaddam *et al.* [18] distinguish cell types by their geometry, and determine the distribution of cell wall thickness and porosity for each cell type in each specimen, and Mayo *et al.* [23] measure porosity and orientation of cells in earlywood and latewood. They do not measure the length of the cells, which requires scans with both sufficient resolution to distinguish the cell walls, and sufficient length along the longitudinal axis of the cells to see their full extent. This is a challenge for cells which can have an aspect ratio of 100 or more.

Cell length and diameter in softwood and hardwood has been widely reported before. One way of generating these data is the time-consuming process of manually measuring cells from physically and chemically macerated wood under a light microscope [24]. Alternatively, optical fibre analysers are used, which allow a rapid and automated analysis of samples, and this technique has been used to build up a picture of fibre geometry across different species [25,26] and throughout a complete tree [27]. These studies show that cell length varies from the centre of the tree, increasing through the juvenile wood and becoming relatively constant in mature wood. Fibre analysers operate on wood pulp, thus losing the structure and arrangement of the material before measurement [25].  $\mu$ CT scanning offers the opportunity to rapidly measure the geometry of hundreds of cells throughout a volume of intact wood.

In this study, three-dimensional scans are used to enable characterization of cell morphometry throughout a series of volumes covering a complete growth ring, and several complete cell lengths. These scans were carried out specifically to estimate the porosity of the wood, the distributions of lumen cross-sectional area and the length of the cells in a set of specimens for which fluid impregnation tests were conducted by BurrIDGE *et al.* [28].

Darcy's Law describes fluid flow in porous media by their permeability, the driving pressure and the viscosity of the fluid. It has been shown to be inaccurate to represent flow in wood by this single permeability parameter [29,30]. The field is rather less developed than the structural analysis of wood, and the progress through multi-scale modelling is less advanced. Zillig *et al.* [31] and Mendoza *et al.* [32]

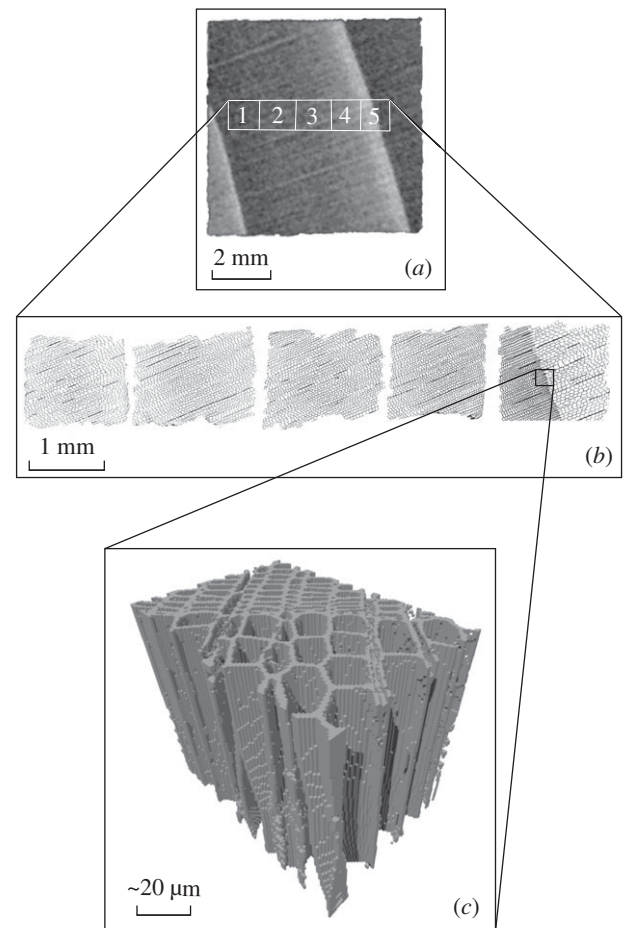
develop meso-scale models representing earlywood and late-wood, cross-grain transport and grain angle. The thesis of Zillig [33] moves towards multi-scale modelling, concluding that ‘in modelling of liquid transport, the cellular level needs to be taken into account’.

The model by Petty [34] is based on the physical micro-structure of the wood. The set of models by Burridge *et al.* [28] extend that of Petty [34] by incorporating capillary action and a statistical representation of the parameters of the cell geometry of the wood, including lumen area and cell length, and their variation through the ring structure. The methods in the present study provide those geometrical parameters, and their statistical distributions at locations across the ring structure of the wood.

Although our specimens were small (10 mm × 10 mm × 70 mm in the longitudinal direction of the cells) compared with wood sections used in structural applications, they contained more than one growth ring, and thus captured a large variation in cell geometry. As with structural-size timber, a scan with sufficient resolution to show the cellular structure across the whole specimen was not feasible either in terms of scan time or data storage capacity. For example, the sub-specimen used for cell length measurement had a file size of 12 GB when reconstructed with 8-bit resolution, and had a scan time of approximately 20 h, and its volume was three orders of magnitude smaller than the complete specimen. We, therefore, first carried out scans with a low resolution, covering the entirety of each specimen, and then cut up those specimens to allow additional high-resolution scans to provide data for the geometry of the cells. We then examined the relationship between data gathered from low-resolution scans and the measured cell geometry from our high-resolution scans, correlating the two to allow an estimation of the variation of cellular geometry across the whole specimen. As a result, this analysis provides measurements of tracheid geometry throughout the ring structure of a softwood.

## 2. Material and methods

The wood used in this study was kiln-dried Sitka spruce (*Picea sitchensis*) supplied by BSW Timber Ltd (Newbridge, Wales). Its moisture content was measured by the oven-dry method to be approximately 12%. Three specimens, 10 mm × 10 mm × 70 mm in the longitudinal direction, were CT-scanned at low resolution over their entire volumes. The three-dimensional image of the specimen is made up of cubic voxels (three-dimensional pixels), which for this scan had a side length of 52.73 µm. The output of the scan is the X-ray attenuation coefficient for each voxel, which is proportional to the mean density of material in that volume. Each specimen was weighed and its dimensions measured before scanning, so that its weight and dimensions could be used to calibrate the correlation between their measured X-ray attenuation coefficient and CT number. The measured bulk density of each specimen was compared to the mean attenuation coefficient of its image, and there was sufficient variation in density between the three specimens to validate this calibration. The high-resolution scan required a smaller sub-specimen, for which a 15 mm length section along the grain was removed from each specimen. A grid was scored onto the surface to enable accurate location of the sub-specimens to be cut from these 15 mm lengths. The sub-specimens were approximately 1.5 mm × 1.5 mm × 15 mm along the grain. The sub-specimens were then cut using a razor blade through the score lines. An



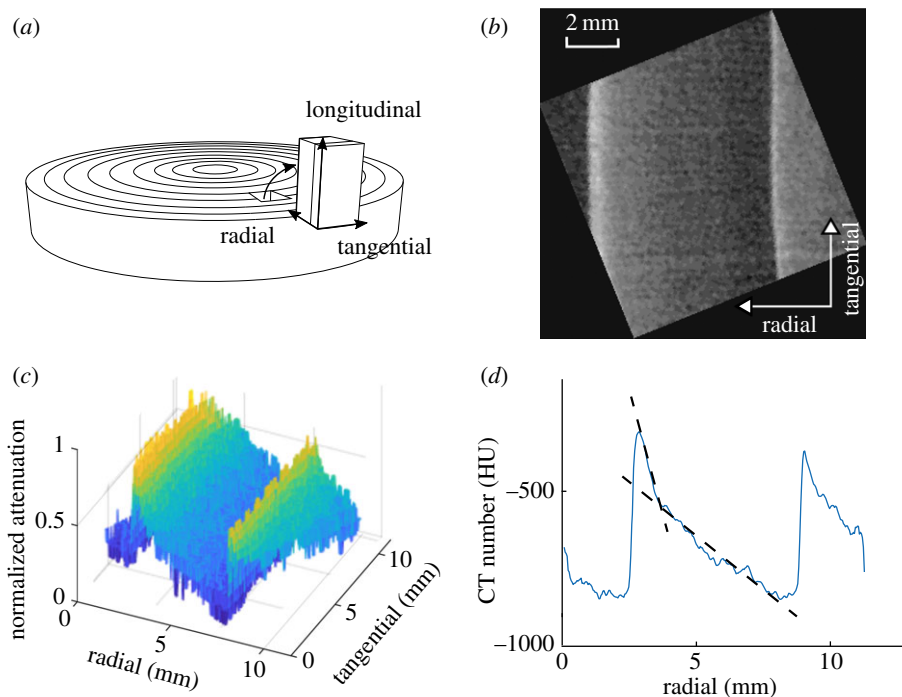
**Figure 1.** Relating specimens and scans across scales, to correlate whole-specimen scans with the measured cellular geometry. Panel (a) is a slice from the low-resolution scan of specimen 2 (light greys mark the highest densities), (b) shows a line of the high-resolution scans on the sub-specimens taken from that specimen (as the solid cell walls are black, the highest density appears darker here) and (c) shows a three-dimensional rendering of all the voxels identified as being part of the cell wall in a small volume of material.

image was taken of the scored grid, which was transferred onto the low-resolution scan, as shown in figure 1a. High-resolution scans were then carried out on these sub-specimens, with a voxel of sides approximately 2 µm. Slices from five of the high-resolution scans are shown in figure 1b. This process ensured that the position of each high-resolution scan was known within the volume of the corresponding low-resolution scan. For the high-resolution scans, the three-dimensional cell geometry could be identified (such as in figure 1c) with every voxel assigned either to be part of the solid cell wall or void space.

### 2.1. Low-resolution scans of the ring structure

For the low-resolution scan, all three specimens were imaged together to ensure the most accurate comparison of the linear attenuation coefficient measured by CT for each specimen. The method is described in §2. The linear attenuation coefficient could then be converted to a CT number using the measured weight of each specimen and its dimensions. As the voxel size for these scans was too large to identify the cell walls individually, the CT number was used to indicate the proportion of solid material and void space in each voxel, or alternatively the porosity. The true porosity in each region was then found using the high-resolution scans on sub-specimens and correlated with the CT number at low resolution. The specimens were identified and separated, and images of individual specimens





**Figure 2.** Panel (a) shows the orientation of the radial, tangential and longitudinal directions in a slice of the trunk. CT scan data at low resolution in (b) and (c) show the variation in CT number across ring structure—dotted lines in (d) show the gradients of linear fits to particular regions. The wood was laid down from right to left by the tree. (Online version in colour.)

were rotated so that the ring structure was aligned with the pixel coordinates for ease of processing and analysis. Figure 2a defines the axes used to describe the orientation of specimens and images in this paper. The radial, tangential and longitudinal planes are defined as the planes to which the axes are normal. Across the 10 mm × 10 mm face of the specimen, the curvature of the rings was not significant, and the variation in CT number due to the rings could therefore be considered to occur along the radial direction. As shown in figure 2b,c, with the rings aligned vertically, there is no apparent systematic variation of CT number in the tangential direction, so the noise can be dealt with most simply by averaging along this direction, giving a mean variation of density across the ring structure as shown in figure 2d.

The variation in CT number across the cross section is shown in figure 2d. The cells at the right-hand edge of the image were grown first. Moving from right to left, the (volumetric) growth rate slows as the tree lays down latewood cells and the CT number increases to a peak (thin vertical white band). The growth then stopped over winter, before restarting in spring at a rapid growth rate as the tree laid down new earlywood cells, with a higher porosity, resulting in a lower CT number (vertical dark band in figure 2b). The CT number then increases gradually towards the next peak, and so on. There is, therefore, a clear boundary between latewood and earlywood in each ring as illustrated by the sharp changes from high to low values of CT number shown in figure 2d, which we refer to as the ‘winter transition’.

Conversely, as the wood cells are laid down during a given growing season, the change from earlywood to latewood is gradual. Havimo *et al.* [35] use the radial diameter of tracheids to measure this gradual transition between earlywood and latewood in Norway Spruce. They note that there is a change in gradient between the two phases, with a much lower gradient in the earlywood phase. Figure 2d shows that a change in the gradient of CT number with radial position is apparent at approximately −525 HU in these specimens, but the data also shows that there is still a marked gradient throughout the earlywood. From all of our low-resolution scan data, the midpoint between the extremes of

CT number is at approximately −525 HU. Throughout, we define the threshold between earlywood and latewood to occur at a CT number of −525 HU.

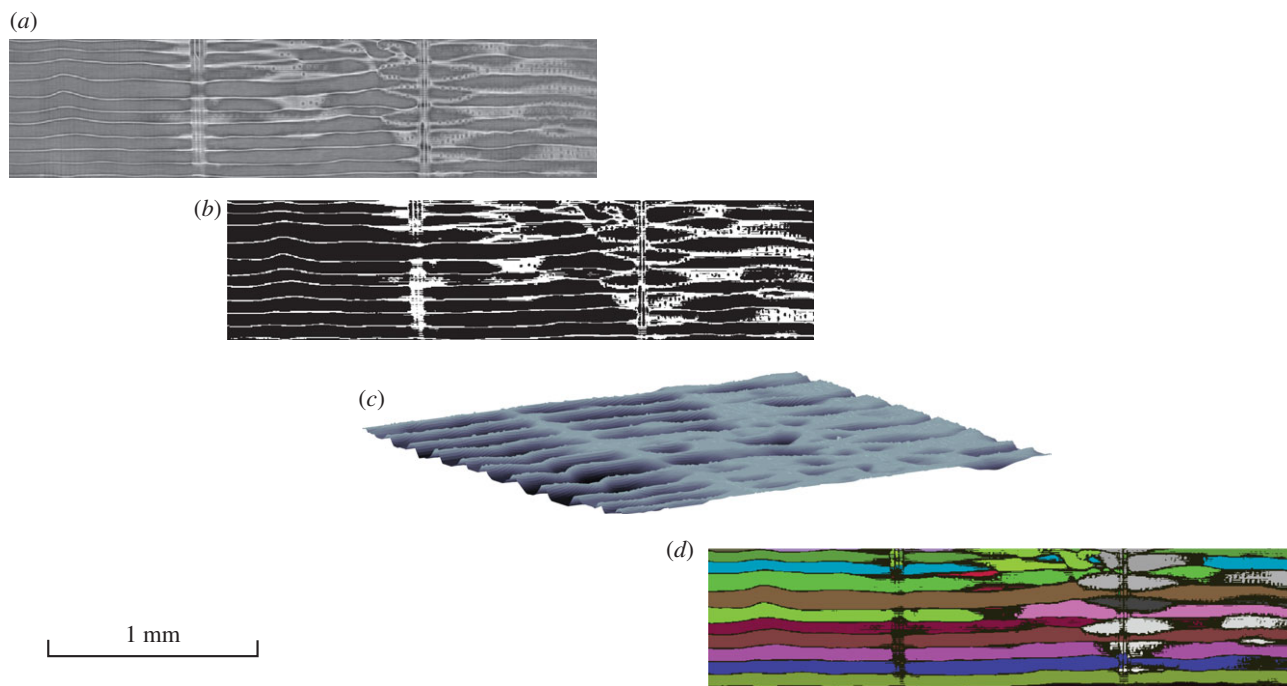
## 2.2. High-resolution scans of the cellular geometry

The  $\mu$ CT method is described in §2. A total of seven sub-specimens were scanned. An image segmentation process was used on the three-dimensional  $\mu$ CT images, to identify each of the tracheid cells, and to assign each voxel either to a cell lumen, or to the cell wall. The segmentation is based on a three-dimensional watershed transform of the image stack produced by CT (also applied to plant cells by Willis *et al.* [36]). The segmented image was then used to measure the dimensions of each cell lumen. The analysis comprised a 6.4 mm-long scan crossing the winter transition between earlywood and latewood, which showed a number of complete cells sufficient for the statistical distribution of their length to be ascertained and compared between earlywood and latewood. In addition, a series of six 2 mm-long scans at varied radial locations and from different specimens enabled the variation of the small-scale geometry across the ring structure to be determined.

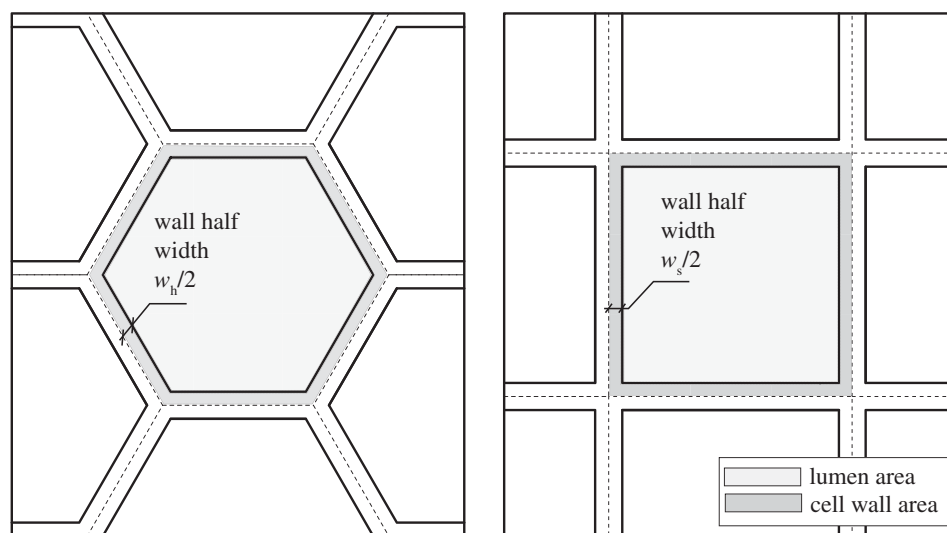
## 2.3. Morphometry analysis

The steps of the image processing are shown in figure 3. These two-dimensional images show the tangential plane, as defined in figure 2a, and illustrate the three-dimensional segmentation process. The detailed process of producing a binary image of solid cell wall material and void space, applying a Euclidian distance transform and then carrying out watershed segmentation is described in electronic supplementary material, S1.

For each high-resolution scan, the distribution of each measured parameter could then be assessed. The mean cross-sectional area of the cell was estimated by dividing its volume (measured as the number of voxels assigned to that cell) by its length (the distance between the furthest spaced voxels). The aspect ratio is estimated as  $L/\sqrt{A}$ , where  $A$  is the cross-sectional area of the lumen and  $L$  is the length. A representative cross-



**Figure 3.** The main steps of the segmentation process: (a) shows the raw greyscale image data from the CT scan; (b) is the binarized image in which cell wall material is distinguished from pore space; (c) is the Euclidian distance transform of the binary image, used for segmentation and (d) is the segmented image, with cell lumina assigned a random colour.



**Figure 4.** Simplified cell geometry assuming either a regular hexagonal cell or a square, showing the lumen and cell wall area assigned to a particular cell.

sectional area for each cell lumen was calculated by dividing the volume of the lumen by its length. This gave an advantage over two-dimensional methods which take a set of measurements at a plane, and thus measure some cell lumina at their tapered ends. Some 'cells' identified by segmentation were radial cells or artefacts of the analysis, and hence the aspect ratio was used to separate out the slender, longitudinal tracheid cells which provide the main structural function and flow paths in the material. Cells with an aspect ratio less than 10 were removed before analysis.

The width of the cell wall can be estimated from the porosity and the number density of cells in the cross section, by assuming a cell shape. Two possible assumed cell shapes, a regular hexagon and a square, are shown in figure 4. These represent two extremes of geometry used for micromechanical modelling of cells [7]. The combined area of the lumen and the cell wall  $A_c$  is given by the inverse of the number density of cells in cells per  $\text{mm}^2$ . The area of the cell wall  $A_w$  is then given by

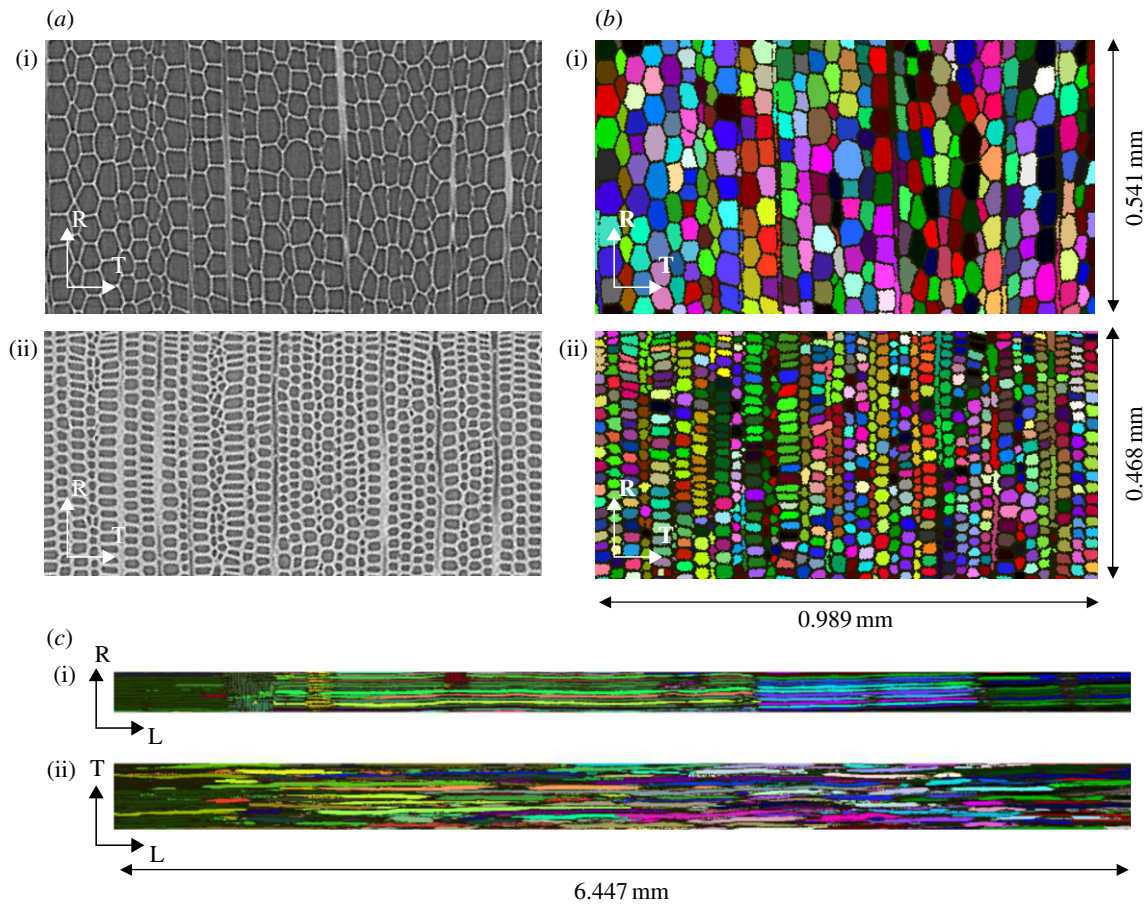
$A_w = (1 - p)A$ , where  $p$  is the porosity. The geometry of the cell for either assumed shape provides an equation for the cell wall thickness  $w$ ,

$$w_h = \sqrt{\frac{2A}{\sqrt{3}}(1 - \sqrt{p})} \quad \text{and} \quad w_s = \sqrt{A(1 - \sqrt{p})}, \quad (2.1)$$

where the subscripts 'h' and 's' correspond to the hexagonal or square shape, respectively. The wall thicknesses calculated for the two geometries differ by less than 8%.

### 3. Results and discussion

Figure 5a shows the cross section of the  $\mu\text{CT}$  image either side of the winter transition, and the corresponding segmented image for each is shown in figure 5b, with each cell assigned a random colour. Figure 5c shows the segmentation



**Figure 5.** Segmented images: (a) the original CT scan data for the earlywood (i) and latewood (ii) side of the winter transition; (b) the corresponding segmented images, with cells identified with a random colour and (c) a longitudinal view showing the full length of the cells in latewood for a tangential (i) and radial (ii) section. R indicates the radial direction, T the tangential and L the longitudinal.

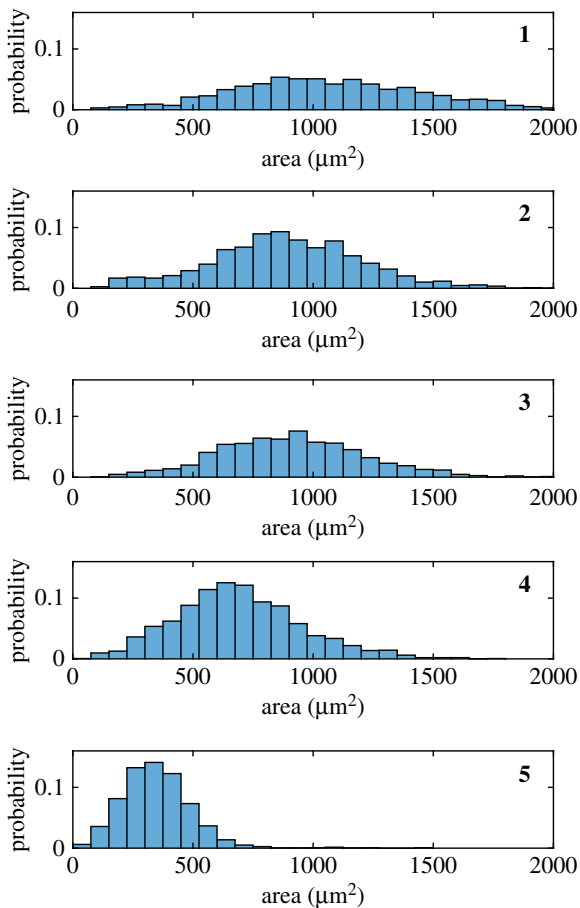
result from the scan covering the longest length along the cell axis. Figure 5c(i) shows the tangential plane, in which each cell is aligned with the ones either side of it, because they are produced from the same parent cell in the cambium of the tree as it increases in diameter. In the lower image, a section at  $90^\circ$  to the one above it showing the radial plane, the cells overlap and are randomly arranged. This is characteristic of Sitka spruce, because the parent cells are arranged with overlap. Species with this feature are described as having a *non-storied* cambium. This illustrates one of the benefits of this method over analysis based on two-dimensional images. As noted by Sarn *et al.* [37], for a non-storied cambium, the random arrangement of cells in the radial plane means that any two-dimensional section of the wood in the longitudinal plane will generally include cells cut through near their narrow tip, and this will give an underestimate of the cross-sectional area of that cell. By considering the entire volume of each cell, we measure a representative cross-sectional area over its whole length, and thus avoid this problem.

Once the cells were identified in the high-resolution scans, and their position in the low-resolution scan was known, it was possible to examine the relationship between position in the ring structure and cell morphometry. Figure 6 shows the histograms of lumen cross-sectional area for five neighbouring regions of wood, together spanning an entire growth ring, from the first earlywood at 1 to the latewood (up to the winter transition) at 5. The histograms show a systematic decrease in the mean area from 1 to 5. This is consistent with the low-resolution data in figure 2d which showed no plateau of CT number in the ring structure to

suggest a homogeneous region of either earlywood or latewood. However, panels 1 to 3 in figure 6 show that the variation in mean area of cell lumen across the earlywood part of the ring is small compared with the variability in each histogram. Expressing these three volumes as a single phase of wood could be reasonable in certain applications. In panels 4 and 5, a contrast is evident moving into the latewood region, with a substantial reduction in the mean area of lumina, and in the variance of area.

The distributions of cell dimensions were then linked to the value of the CT number measured at the same point in the specimen in the low-resolution scans. Having measured the total volume associated with lumina within our high-resolution scans, we could calculate the porosity of any given region. Figure 7b shows the variation of measured porosity with CT number. Each datum represents the mean of one complete high-resolution scan. Assuming that the material density of the solid cell wall does not vary (for example with porosity), a linear relationship between CT number and porosity is expected. The data show reasonable agreement with a linear relationship (figure 7b) and hence we regard this assumption to be valid. The least-squares fitted linear relationship in figure 7b has a CT number of 712 HU for a porosity of zero, equivalent to a bulk density of  $1712 \text{ kg m}^{-3}$ . The oven dry density of the solid cell wall in softwood is approximately  $1500 \text{ kg m}^{-3}$  [38], and increases with moisture content [39]. The moisture content of these specimens, at 12%, would not result in a 12% increase in cell wall density, because of swelling of the cell wall, but the intercept for zero porosity is likely to be within 10% of the expected value.





**Figure 6.** Histograms of lumen cross-sectional area from high-resolution scan on sub-specimens **1** to **5** from specimen **2**, shown in figure **1(a)**—only the latewood part of **5**, before the winter transition, is included. (Online version in colour.)

The greyscale images were converted to binary cell wall–void space using a threshold filter based on the average intensity in the region. This means that in regions with high cell wall content, and therefore high intensity, the binary threshold is raised slightly, leading to a tendency to increase the measured porosity. This would tend to change the gradient of the fitted relationship, and result in a higher value of the intercept for zero porosity. The observation that the fitted curve has an intercept for zero porosity close to the expected cell wall density gives some confidence that any artificial increase in porosity in areas of high cell wall content is not severe.

The total void space in a given cross section may also be calculated by multiplying the mean (cross-sectional) area of cell lumina (for example in  $\text{mm}^2$ ) by the number density of cells (for example in  $\text{mm}^{-2}$ ). This procedure, carried out over a representative sample of cross sections, provides a method for estimating the porosity. Thus, if the relationships between both the area of cell lumina and CT number, and the number density of these cells and CT number, can be approximated by power laws, then the exponents of the two power laws must sum to unity; i.e. the product of the two relationships must be linear (figure **7b**).

The number density of cells within the specimens is approximately  $500 \text{ mm}^{-2}$  in the most porous and increases to approximately  $1000 \text{ mm}^{-2}$  in the least porous wood and hence the exponent in the power law relating these must be greater than zero. Our data for the mean area of the cell

lumina and the number density of cells (figure **7a,c**, respectively) are not sufficient to determine the precise exponent of the power laws. Arbitrarily setting the exponent in both power laws to 0.5 provides a reasonable fit to both datasets—see the green curves in figure **7a,c**—reassuringly, this highlights that our analysis yields results that are not inconsistent with physical constraints. Furthermore, we note that the product of these two power laws yields a linear fit between the porosity and CT number which is approximately 10% lower than the results plotted in figure **7b**; this difference is to be expected, because we deliberately included only tracheid cells in our analysis of the high-resolution scan data and thereby excluded the pore space associated with, for example, ray cells. Within figure **7a**, we plot the best fits for power laws with exponents of 0.5 and 1.0 (i.e. linear). The difference between these two fits (with distinctly different exponents) over the range of values of interest is always less than 5%. For simplicity, we therefore adopt a linear fit to map CT number in the low-resolution scans to a prediction of lumina area.

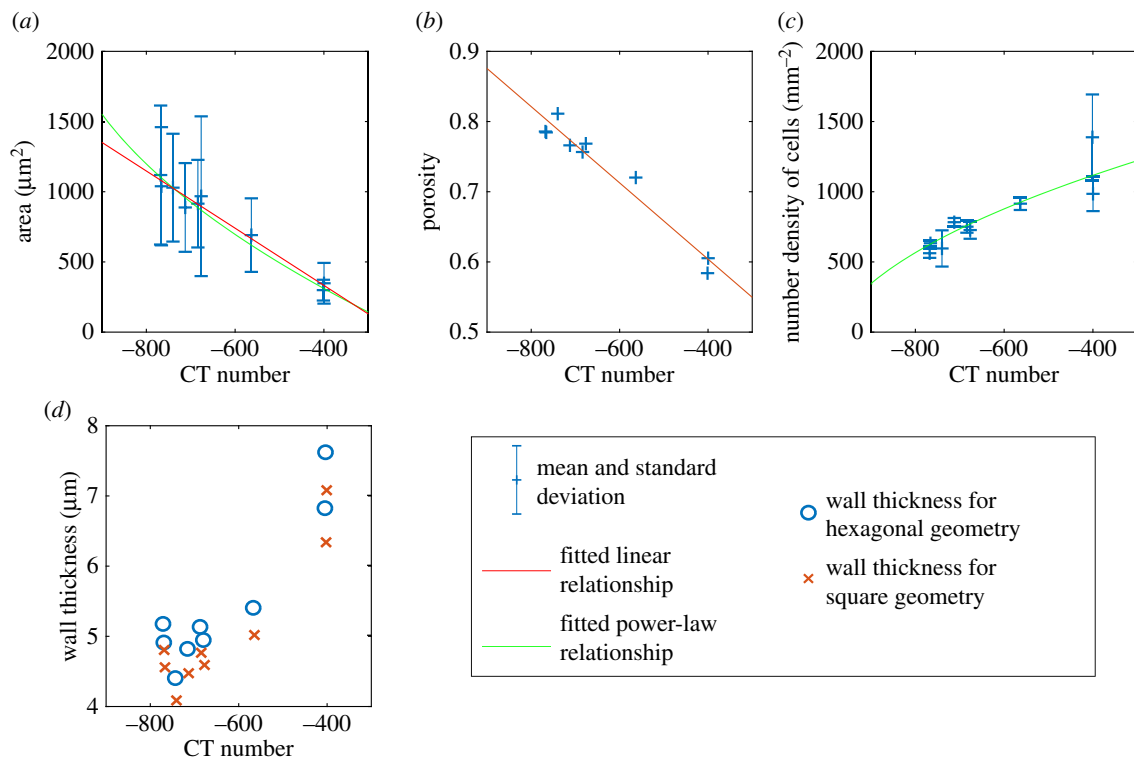
In contrast to the relationship between CT number and porosity, there is not a unique physical relationship between cell lumina area and CT number: the same CT number could result from either a low number density of large lumina with thick cell walls or a high number density of smaller lumina with thin cell walls. The fact that lumen cross-sectional area and CT number are well correlated (figure **7a**) suggests that other fixed patterns in the cellular structure exist, e.g. the cell wall thickness and number density of cells also vary with the porosity (and hence CT number). We hypothesize that the relationships are, in fact, unique within a species or within a species grown in a certain location, and the data we have collected so far support that hypothesis, because the area of cell lumina is proportional to CT number, even within different specimens. A full characterization of the pattern of geometry in the wood requires accurate measurements of those parameters.

The estimates of cell wall thickness calculated using the two methods detailed in equation (2.1) are plotted in figure **7d**, the difference due to the choice of method is of the same order as the variations between sub-specimens of similar porosity/CT number. The data for wall thickness showed too much scatter to justify fitting and mapping onto the low-resolution scans, but they are plotted in figure **7d** to show that such a mapping would be possible given more reliable data on the number density of cells. We assert that a segmentation process which also identifies radial cells could enable this.

The approximate linear relationships determined from the data of the high-resolution scans (figure **7a,b**) were used to map the data from the low-resolution scans onto estimates of both the porosity and lumen areas. In so doing, we were able to provide estimates of the small-scale properties, i.e. lumen areas, for the complete specimens—the data from which are presented in table 1.

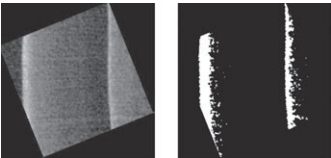

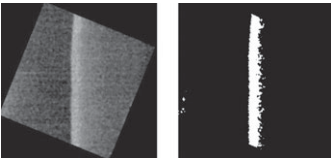
Figure 8 shows that the tracheid length does not vary across the winter transition between earlywood and latewood: the mean length is 2.46 mm for earlywood, with a coefficient of variation of 0.24, and 2.50 mm for latewood, with a coefficient of variation of 0.22. These parameters are taken to be representative for these specimens, and fit within the range for mature wood of 2.1–3.1 mm reported by Brazier [40] for UK-grown Sitka spruce.

The variation in CT number across the specimen does not show a boundary between two separate homogeneous



**Figure 7.** Measured cell geometry: (a–d) show the relationship between CT number in the low-resolutions scans (measured at the relevant location) and the measured cell properties from the high-resolution scans of each of the sub-specimens. Two specimens were split either side of the winter transition, giving nine points. (Online version in colour.)

**Table 1.** Parameters from measured cell geometry mapped onto complete specimens, as mean values with coefficient of variation in brackets where applicable. Areas identified as latewood are shown in white in the right-hand image of each specimen.

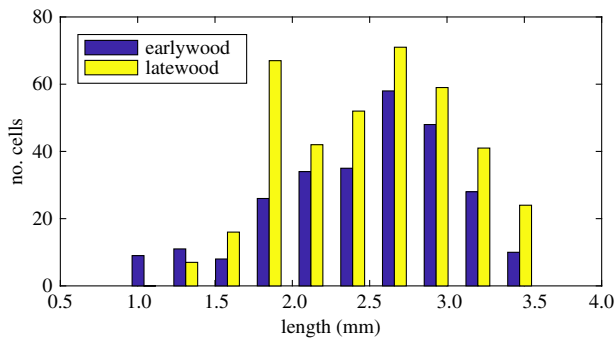
		proportion	porosity	lumen area $\mu\text{m}^2$
specimen 1	entire specimen	—	0.73 (0.09)	787 (0.30)
	earlywood	$\alpha = 0.83$	0.75 (0.06)	867 (0.20)
	latewood	$1 - \alpha = 0.17$	0.63 (0.05)	415 (0.27)
				
specimen 2	entire specimen	—	0.75 (0.08)	869 (0.26)
	earlywood	$\alpha = 0.88$	0.76 (0.05)	930 (0.17)
	latewood	$1 - \alpha = 0.12$	0.63 (0.04)	417 (0.21)
				
specimen 3	entire specimen	—	0.75 (0.07)	873 (0.24)
	earlywood	$\alpha = 0.89$	0.76 (0.05)	923 (0.16)
	latewood	$1 - \alpha = 0.11$	0.63 (0.03)	436 (0.17)
				

phases of less porous ‘latewood’ and ‘earlywood’ in these specimens, but a change in gradient is apparent which can be used to distinguish between the two. For some applications, it may not be necessary to distinguish between phases of wood, because a CT scan can give a CT number

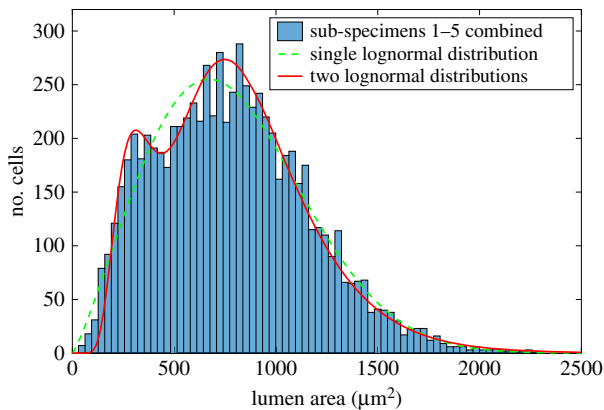
at every point throughout its volume, which may be mapped onto a variation in other properties, such as lumen area and porosity.

For many applications, the distinction between phases is important [28]. Application to flow modelling, for example,





**Figure 8.** Comparison of length measurements of tracheids in adjacent earlywood and latewood volumes. (Online version in colour.)



**Figure 9.** Histogram combining the (7610) lumen areas plotted within figure 6 which span one entire growth ring. The best-fit lognormal distribution is marked by the dashed curve. The distribution obtained by classifying the data into earlywood and latewood phases, fitting each phase to a lognormal distribution, and summing these fits produces the distribution marked by the solid curve. (Online version in colour.)

requires a distinction between earlywood and latewood, because information taken from the literature on the number, geometry and probability of aspiration of bordered pits is specific to earlywood and latewood phases [41–43]. Moreover, for both flow modelling and micromechanical models, even in the absence of the need to consider two distinct phases, it may be necessary to accurately represent the statistical distribution of the microstructure geometry (e.g. cell wall thickness and lumen area), which often proves challenging.

The histogram of the measurements of lumen area across the ring structure from figure 6 (specimen 2, sub-specimens 1–5) is plotted in figure 9. As the areas must follow a single-sided distribution (i.e. take strictly positive values), one might expect to represent the data using, for example, a lognormal distribution (which is relatively common in nature and can be expected under either the central-limit theorem or maximum entropy arguments [44]). However, the fit of the data to a single lognormal distribution is poor. On the other hand, fitting separate lognormal distributions,  $X_e$ , to the lumen areas to each of the earlywood,  $X_e$ , and latewood,  $X_l$ , data provide a simple means of achieving a good fit to the data. Figure 9 shows the fit achieved taking the volume weighted average of the two lognormal distributions according to:  $n[\alpha X_e + (1 - \alpha)X_l]$ , where  $n$  is the number of cells sampled; values for the means and variances of the lognormal distributions, and the value of  $\alpha$  (the proportion of earlywood), are all taken from the data of specimen 2, sub-specimens 1–5.

For each specimen, every voxel can be assigned a porosity and a distribution of lumen cross-sectional area, mapped according to the relationships shown in figure 7. The resulting parameters for earlywood and latewood in each specimen are given in table 1. As expected, these measurements, taken across an entire specimen, do not show such a stark distinction between earlywood and latewood as would be expected for the material immediately to each side of the winter transition, as shown in figure 5. This is because these parameters are the mean for each phase when all of the ring structure is classified as either earlywood or latewood and there is substantial variation in each phase.

The extremes of porosity across the ring structure are better seen in figure 7. At approximately 0.58 and 0.81, they correspond to CT numbers of  $-740$  HU and  $-401$  HU, and bulk densities of  $260$  and  $599 \text{ kg m}^{-3}$ , which fit well within the range of values measured for UK-grown Sitka spruce by Brazier [40].

## 4. Conclusion

We have measured the variation in CT number across the ring structure of softwood specimens using low-resolution scans, and determined the size and shape of softwood tracheids at high resolution, by X-ray  $\mu$ CT and image processing. The subsequent data were used to show the extent to which the CT number measured across the ring structure for low-resolution imaging can be correlated to the geometry of the cellular structure that makes up the wood. Using the correlation between CT number and both porosity and cell cross-sectional area, shown in figure 7, it has been possible to map the measured CT number throughout specimens with complete growth rings onto corresponding values of cross-sectional area and porosity. The correlation between CT number and cell cross-sectional area is not determined by any physical constraint: it appears to be a pattern of growth in the wood. Further research is required to identify the bounds within which this correlation holds: it may be true for all trees of a particular species, or all those grown in a particular climate.

It is intended that this mapping from the cell structure to measurements which could be made at the scale of structural timber provides a step towards linking the bulk engineering properties of timber to its fundamental underlying structure. Ultimately, this would lead to better multi-scale modelling of wood, more rigorous grading of structural timber and more effective design of processes which involve fluid flow through wood, such as impregnation and drying.

We have discussed the merit of describing this wood in terms of earlywood and latewood phases. There is a gradual transition of CT number across an annual ring, and this is reflected in a gradual transition of cell lumen area across the five sub-specimens studied across the ring structure, as shown in figure 6. However, the distribution of lumen areas across the ring as a whole is shown in figure 9 to be well represented by the sum of two lognormal distributions, and this insight may be useful in wood modelling in various fields.

Our finding that there is no significant variation in cell length within the ring structure, shown in figure 8, is reasonable, given that the cells are laid down sequentially by the same initial cells, and this has been shown in previous

studies. This study shows that  $\mu$ CT can provide these data for volumes of intact wood incorporating several hundred cells. This information is crucial in the modelling of fluid transport in wood, because good estimates of the cell lengths and their statistical distribution in different parts of the wood enable a more accurate estimate for the number of bordered pits between cells (which provide the greatest restriction to fluid flow) that fluid must pass through along a given flow path.

**Data accessibility.** Electronic supplementary material describing the segmentation process are included as S1. The greyscale images which form the CT scan data are available at doi:10.7488/ds/2260, along with Matlab code for segmentation.

**Authors' contributions.** T.P.S.R. wrote the majority of the manuscript, conceived and carried out the image segmentation and subsequent

analysis. H.C.B. and T.P.S.R. developed the strategy for data fitting, mapping between scales and statistical analysis and wrote those parts of the manuscript. R.J. planned and carried out the scanning, reconstruction and processing of the CT scans, and wrote S2. G.W., D.U.S., O.A.S., P.F.L. and M.H.R. provided guidance and instruction throughout. All authors reviewed and edited the manuscript throughout its development.

**Competing interests.** The authors have no competing interests.

**Funding.** This work was funded in major part by a Leverhulme Trust Programme Grant. The X-ray imaging work was supported by the Advanced Imaging of Materials (AIM) facility (EPSRC grant no. EP/M028267/1), the European Social Fund (ESF) through the European Union's Convergence programme administered by the Welsh Government.

**Acknowledgements.** Thanks are expressed to Yassin Refahi of INRA for his insight into applying image segmentation to plants.

## References

- Siau JF. 1984 *Transport processes in wood*. Berlin, Germany: Springer.
- Ramage MH *et al.* 2017 The wood from the trees: the use of timber in construction. *Renew. Sustain. Energy Rev.* **68**, 333–359. (doi:10.1016/j.rser.2016.09.107)
- Bjurhager I. 2008 Mechanical behaviour of hardwoods—effects from cellular and cell wall structures. PhD thesis, Royal Institute of Technology (KTH), Sweden.
- Gibson LJ. 2012 The hierarchical structure and mechanics of plant materials. *J. R. Soc. Interface* **9**, 2749–2766. (doi:10.1098/rsif.2012.0341)
- Qing H, Mishnaevsky L. 2010 3D multiscale micromechanical model of wood: from annual rings to microfibrils. *Int. J. Solids Struct.* **47**, 1253–1267. (doi:10.1016/j.ijsolstr.2010.01.014)
- Malek S, Gibson LJ. 2017 Multi-scale modelling of elastic properties of balsa. *Int. J. Solids Struct.* **113–114**, 118–131. (doi:10.1016/j.ijsolstr.2017.01.037)
- Mishnaevsky L, Qing H. 2008 Micromechanical modelling of mechanical behaviour and strength of wood: state-of-the-art review. *Comput. Mater. Sci.* **44**, 363–370. (doi:10.1016/j.commatsci.2008.03.043)
- Hofstetter K, Gamstedt EK. 2009 Hierarchical modelling of microstructural effects on mechanical properties of wood. A review. COST Action E35 2004–2008: wood machining—micromechanics and fracture. *Holzforchung* **63**, 130–138. (doi:10.1515/HF.2009.018)
- de Borst K, Bader TK, Wikete C. 2012 Microstructure—stiffness relationships of ten European and tropical hardwood species. *J. Struct. Biol.* **177**, 532–542. (doi:10.1016/j.jsb.2011.10.010)
- De Borst K, Bader TK. 2014 Structure—function relationships in hardwood—insight from micromechanical modelling. *J. Theor. Biol.* **345**, 78–91. (doi:10.1016/j.jtbi.2013.12.013)
- Ridley-Ellis D, Stapel P, V Babo. 2016 Strength grading of sawn timber in Europe: an explanation for engineers and researchers. *Euro. J. Wood Wood Products* **74**, 291–306. (doi:10.1007/s00107-016-1034-1)
- Zauner M, Keunecke D, Mokso R, Stampanoni M, Niemz P. 2012 Synchrotron-based tomographic microscopy (SbTM) of wood: development of a testing device and observation of plastic deformation of uniaxially compressed Norway spruce samples. *Holzforchung* **66**, 973–979. (doi:10.1515/hf-2011-0192)
- Baensch F, Zauner M, Sanabria SJ, Sause MGR, Pinzer BR, Brunner AJ, Stampanoni M, Niemz P. 2015 Damage evolution in wood: synchrotron radiation micro-computed tomography (SR $\mu$ CT) as a complementary tool for interpreting acoustic emission (AE) behavior. *Holzforchung* **69**, 1015–1025. (doi:10.1515/hf-2014-0152)
- Schad KC, Schmoldt DL, Ross RJ. 1966 Nondestructive methods for detecting defects in softwood logs. Technical report, Forest Products Laboratory, Madison, WI.
- Sterley M, Serrano E, Enquist B, Hornatowska J. 2013 Finger jointing of freshly sawn Norway spruce side boards—a comparative study of fracture properties of joints glued with phenol—resorcinol and one-component polyurethane adhesive. In *Materials and joints in timber structures*. RILEM Bookseries, vol. 9. (eds S Aicher, HW Reinhardt, H Garrecht), pp. 325–339. Dordrecht, The Netherlands: Springer.
- Fromm JH, Sautter I, Matthies D, Kremer J, Schumacher P, Ganter C. 2001 Xylem water content and wood density in spruce and oak trees detected by high-resolution computed tomography. *Plant. Physiol.* **127**, 416–425. (doi:10.1104/pp.010194)
- Žlahtič M, Mikac U, Sešša I, Merela M, Humar M. 2017 Distribution and penetration of tung oil in wood studied by magnetic resonance microscopy. *Ind. Crops. Prod.* **96**, 149–157. (doi:10.1016/j.indcrop.2016.11.049)
- Sedighi Moghaddam M, Van den Bulcke J, Wälinder ME, Claesson PM, Van Acker J, Swerin A. 2017 Microstructure of chemically modified wood using X-ray computed tomography in relation to wetting properties. *Holzforchung* **71**, 201. (doi:10.1515/hf-2015-0227)
- Derome D, Zillig W, Carmeliet J. 2009 Multi-scale modeling for moisture transport in wood. In *Proc. Sixth Plant Biomechanics Conf.*, 16–21 November, Cayenne, French Guyana, pp. 53–58. Cayenne, French Guyana: UMR EcoFoG.
- Bouche PS *et al.* 2016 Are needles of *Pinus pinaster* more vulnerable to xylem embolism than branches? New insights from X-ray computed tomography. *Plant Cell Environ.* **39**, 860–870. (doi:10.1111/pce.12680)
- Zauner M, Stampanoni M, Niemz P. 2016 Failure and failure mechanisms of wood during longitudinal compression monitored by synchrotron micro-computed tomography. *Holzforchung* **70**, 179–185. (doi:10.1515/hf-2014-0225)
- Steppe K, Cnudde V, Girard C, Lemeur R, Cnudde JP, Jacobs P. 2004 Use of X-ray computed microtomography for non-invasive determination of wood anatomical characteristics. *J. Struct. Biol.* **148**, 11–21. (doi:10.1016/j.jsb.2004.05.001)
- Mayo SC, Chen F, Evans R. 2010 Micron-scale 3D imaging of wood and plant microstructure using high-resolution X-ray phase-contrast microtomography. *J. Struct. Biol.* **171**, 182–188. (doi:10.1016/j.jsb.2010.04.001)
- Fujiwara S, Yang KC. 2000 The relationship between cell length and ring width and circumferential growth rate in five Canadian species. *IAWA J.* **21**, 335–345. (doi:10.1163/22941932-90000251)
- Li B, Bandekar R, Zha Q, Alsagga A, Ni Y. 2011 Fiber quality analysis: opTest fiber quality analyzer versus L&W fiber tester. *Ind. Eng. Chem. Res.* **50**, 12 572–12 578. (doi:10.1021/ie201631q)
- Mvolo CS, Koubaa A, Beaulieu J, Cloutier A, Mazerolle MJ. 2015 Variation in wood quality in white spruce (*Picea glauca* (Moench) Voss). Part I. Defining the juvenile—mature wood transition based on tracheid length. *Forests* **6**, 183–202. (doi:10.3390/f6010183)

27. Yemele MC, Beaulieu J, Defo M, Koubaa A, Cloutier A, Mvolo CS. 2015 Prediction of tracheid length and diameter in white spruce (*Picea glauca*). *IAWA J.* **36**, 186–207. (doi:10.1163/22941932-00000095)
28. Burrige H, Wu G, Reynolds TPS, Shah D, Johnston R, Scherman OA, Ramage MH, Linden PF. Submitted. The liquid transport in softwood: timber as a model porous medium and natural material. *Proc. Natl Acad. Sci. USA*.
29. Bramhall G. 1971 The validity of Darcy's law in the axial penetration of wood. *Wood Sci. Technol.* **5**, 121–134.
30. Banks WB. 1981 Addressing the problem of non-steady state liquid flow in wood. *Wood Sci. Technol.* **15**, 171–177.
31. Zillig W, Janssen H, Carmeliet J, Derome D. 2006 Liquid water transport in wood: towards a mesoscopic approach. In *Research in building physics and building engineering* (eds P Fazio, H Ge, J Rao, G Desmarais), pp. 107–114. London, UK: Taylor & Francis.
32. Mendoza M, Hass P, Wittel FK, Niemz P, Herrmann HJ. 2012 Adhesive penetration of hardwood: a generic penetration model. *Wood Sci. Technol.* **46**, 529–549.
33. Zillig W. 2009 Moisture transport in wood using a multiscale approach. PhD thesis, Katholieke Universiteit Leuven.
34. Petty J. 1970 Permeability and structure of the wood of Sitka spruce. *Proc. R. Soc. Lond. B* **175**, 149–166. (doi:10.1098/rspb.1970.0016)
35. Havimo M, Rikala J, Sirviö J, Sipi M. 2008 Distributions of tracheid cross-sectional dimensions in different parts of Norway spruce stems. *Silva Fennica* **42**, 89–99.
36. Willis L, Refahi Y, Wightman R, Landrein B, Teles J, Huang KC, Meyerowitz EM, Jönsson H. 2016 Cell size and growth regulation in the *Arabidopsis thaliana* apical stem cell niche. *Proc. Natl Acad. Sci.* **113**, E8238–E8246. (doi:10.1073/pnas.1616768113)
37. Sarén MP, Serimaa R, Andersson S, Paakkari T, Saranpää P, Pesonen E. 2001 Structural variation of tracheids in Norway spruce (*Picea abies* [L.] Karst.). *J. Struct. Biol.* **136**, 101–109. (doi:10.1006/jsbi.2001.4434)
38. Moore J. 2011 Wood properties and uses of Sitka spruce in Britain. Technical report, Edinburgh, Jan 2011.
39. Zauer M, Pfriem A, Wagenführ A. 2013 Toward improved understanding of the cell-wall density and porosity of wood determined by gas pycnometry. *Wood. Sci. Technol.* **47**, 1197–1211. (doi:10.1007/s00226-013-0568-1)
40. Brazier JD. 1967 Timber Improvement II: the effect of vigour on young-growth Sitka spruce. *Forestry* **40**, 117–128. (doi:10.1093/forestry/40.2.117)
41. Phillips EWJ. 1933 Movement of the pit membrane in coniferous woods, with special reference to preservative treatment. *Forestry* **7**, 109–120. (doi:10.1093/oxfordjournals.forestry.a063340)
42. Liese W, Bauch J. 1967 On the closure of bordered pits in conifers. *Wood. Sci. Technol.* **1**, 1–13. (doi:10.1007/BF00592252)
43. Ahmed SA, Hansson L, Morén T. 2013 Distribution of preservatives in thermally modified scots pine and norway spruce sapwood. *Wood. Sci. Technol.* **47**, 499–513. (doi:10.1007/s00226-012-0509-4)
44. Lyon A. 2013 Why are normal distributions normal? *Br. J. Philos. Sci.* **65**, 621–649. (doi:10.1093/bjps/axs046)